Article

Breaking shackles of molecular weight and emission for NIR-II fluorophores by regulating Columb attraction interaction

Miantai Ye[1,2,3,4,5,6,8], Xiaoyu Wang[1,2,8], Jingwen Zou[1,2,8], Wei Sun[4,5,6], Weijie Chi ®[7] ✉, Zhiqiang Mao ®[1,2] ✉ & Zhihong Liu ®[1,2,3] ✉

The second near-infrared (NIR-II) dyes provide advantages for in vivo imaging, but challenges persist. A primary issue is the lack of practicable strategies to balance emission wavelength and molecular weight, particularly for low-molecular-weight (<500 Da) NIR-II (λ_{em} > 1000 nm) dyes. Here, we propose a strategy that tunes NIR-II emissions by reducing Coulomb attraction interaction, contrasting with traditional approaches that redshift absorption wavelengths through energy gap reduction. Leveraging this concept, we extend the emission wavelength of GFP chromophore-based dyes LS1-12 from the visible range into the NIR-II region, achieving a maximum emission wavelength exceeding 1200 nm with molecular weights between 226 and 449 Da. Further, the optimized NIR-II dye LS7 selectively binds $A\beta_{42}$ fibrils, yielding a 22.7-fold fluorescence increase in vitro and enabling real-time imaging of deposited Aβ proteins in the brains of living mice with Alzheimer's disease. This study introduces a distinct design strategy for low-molecular-weight NIR-II dyes and addresses a longstanding bottleneck in this field.

The second near-infrared (NIR-II, 1000–1700 nm) fluorescence imaging is advantageous for in vivo studies of various diseases, providing reliable data support for disease diagnosis, prognosis, and treatment. Its benefits include low spontaneous background interference, deep tissue penetration, high spatial resolution, and high signal-to-noise ratio[1–5]. Among the numerous NIR-II fluorescent contrasts, organic small molecule dyes demonstrated substantial potential for clinical translation owing to their tunable optical properties and superior biocompatibility[6–9]. Several NIR-II molecular dyes have been reported, including polymethine, bibenzo-thiazole, BODIPY, and anthraquinone-based dyes[10–18]. These dyes demonstrate promising applications in vascular localization, respiratory rate measurement, and fluorescence-guided tumor resection. Nonetheless, most of these dyes have high

molecular weights (MW > 500 Da) and poor water solubility, limiting their practical applications. Thus, it is essential to have more effective methods to better balance fluorescence wavelengths and molecular weight for NIR-II dyes.

The general strategy for achieving spectral redshift in organic dyes involves reducing their fundamental band gaps ($\Delta E_{HOMO-LUMO}$), defined as the difference between the ionization potential and electron affinity, by lowering the lowest unoccupied molecular orbital (LUMO) or raising the highest occupied molecular orbital (HOMO)[19–22]. However, these approaches typically rely on enhancing the conjugated systems of planar dyes or increasing the push-pull effect in donor-acceptor dyes, leading to larger molecular sizes[23–26]. While expanding π-conjugation length is a widely used strategy to reduce fundamental

[1]National & Local Joint Engineering Research Center of High-throughput Drug Screening Technology, Hubei University, Wuhan, China. [2]College of Health Science and Engineering, Hubei University, Wuhan, China. [3]College of Chemistry and Molecular Sciences, Wuhan University, Wuhan, China. [4]Hainan Engineering Research Center of Tropical Ocean Advanced Optoelectronic Functional Materials, Hainan Normal University, Haikou, China. [5]Key Laboratory of Laser Technology and Optoelectronic Functional Materials of Hainan Province, Hainan Normal University, Haikou, China. [6]College of Chemistry and Chemical Engineering, Hainan Normal University, Haikou, China. [7]School of Chemistry and Chemical Engineering, Hainan University, Haikou, China. [8]These authors contributed equally: Miantai Ye, Xiaoyu Wang, Jingwen Zou. ✉e-mail: weijie_chi@hainanu.edu.cn; maozq@hubu.edu.cn; zhhliu@whu.edu.cn

band gaps, it is less effective for developing small organic NIR-II emitters compared to visible/NIR-I emitters[27-30]. This is primarily due to the fact that excessively small band gaps often lead to physical/chemical instability and fluorescence quenching, complicating the synthesis and viability of these dyes[31,32]. Besides, in principle, the fundamental band gap is related to the optical gap (absorption peak), which corresponds to the energy of the lowest electronic transition accessible via the absorption of a single photon. A small fundamental band gap causes a lower optical gap (long absorption wavelength). In other words, regulating the fundamental band gap directly results in a change in the absorption peak rather than the emission peak of the molecule[33]. In this scenario, various efforts have been made to extend emission wavelengths by introducing functional groups that modulate the aggregation state of fluorophores, promoting bathochromic shift *J*-aggregation[34-36]. However, *J*-aggregation typically results in a low molar extinction coefficient, a limitation that is difficult to overcome through simple molecular modifications. Additionally, *J*-aggregation imposes stringent structural requirements on the fluorophores[37-40]. An emerging strategy for designing long-wavelength NIR-II dyes involves constructing antiaromatic conjugated systems[41]. It is a well-known fact that antiaromaticity often leads to significantly reduced fluorescence quantum yields.

Herein, we proposed a distinct strategy for modulating NIR-II emission wavelengths of dyes by optimizing their structure to adjust the Coulomb attraction interaction (E_c) of photoluminescent photons. Small E_c suggests a weak interaction of photo-generated electron and hole, which increases the separation efficiency of electron and hole, leading to a long charge transfer distance and enhances the intramolecular charge transfer (ICT) effect. As a result, the small E_c results in a redshift of emission wavelength (Fig. 1A). This strategy also addresses the critical challenge faced by organic small-molecule NIR-II dyes: balancing fluorescence wavelength and molecular weight. Using this design, a spectrum of GFP chromophore-based organic NIR-II dyes were produced, termed LSs, featuring tunable long wavelengths (444–1218 nm) and small molecular weights (226–449 Da) (Table 1). Compared to reported dyes, these LS dyes not only exhibit longer emission wavelengths and larger Stokes shifts (up to 582 nm), but also maintain small molecular sizes (<500 Da) (Figs. 1B, C, S2, S3 and Table S19). Additionally, inspired by the bioluminescence principles of natural fluorescent proteins (FPs), we hypothesized that the hydrophobic cavity of β-amyloid could mimic the β-barrel in FPs, facilitating the formation of dye-protein complexes through multiple noncovalent interactions. The complexes would exhibit enhanced fluorescence intensity, allowing for the specific detection of β-amyloid[42-46]. As a proof of concept, LS7 demonstrated the highest specificity for β-amyloid after dye screening, enabling real-time in vivo NIR-II fluorescent detection of β-amyloid in the Alzheimer's disease (AD) mouse brains.

Results

Molecular design and synthesis

Currently, most research has focused on developing NIR-II emission dyes by red-shifting absorption via reduced fundamental band gaps ($\Delta E_{\text{HOMO-LUMO}}$), lacking strategies to directly redshift the emission spectra. The Coulomb attraction interaction of electron and hole has a great effect on the ICT in the excited state of the dye. Poor Coulomb attraction interaction enhances the ICT and increases the emission wavelength of the dye. Thus, optimizing molecular structures to reduce the Coulomb attraction interaction would be a desired strategy for developing NIR-II dyes.
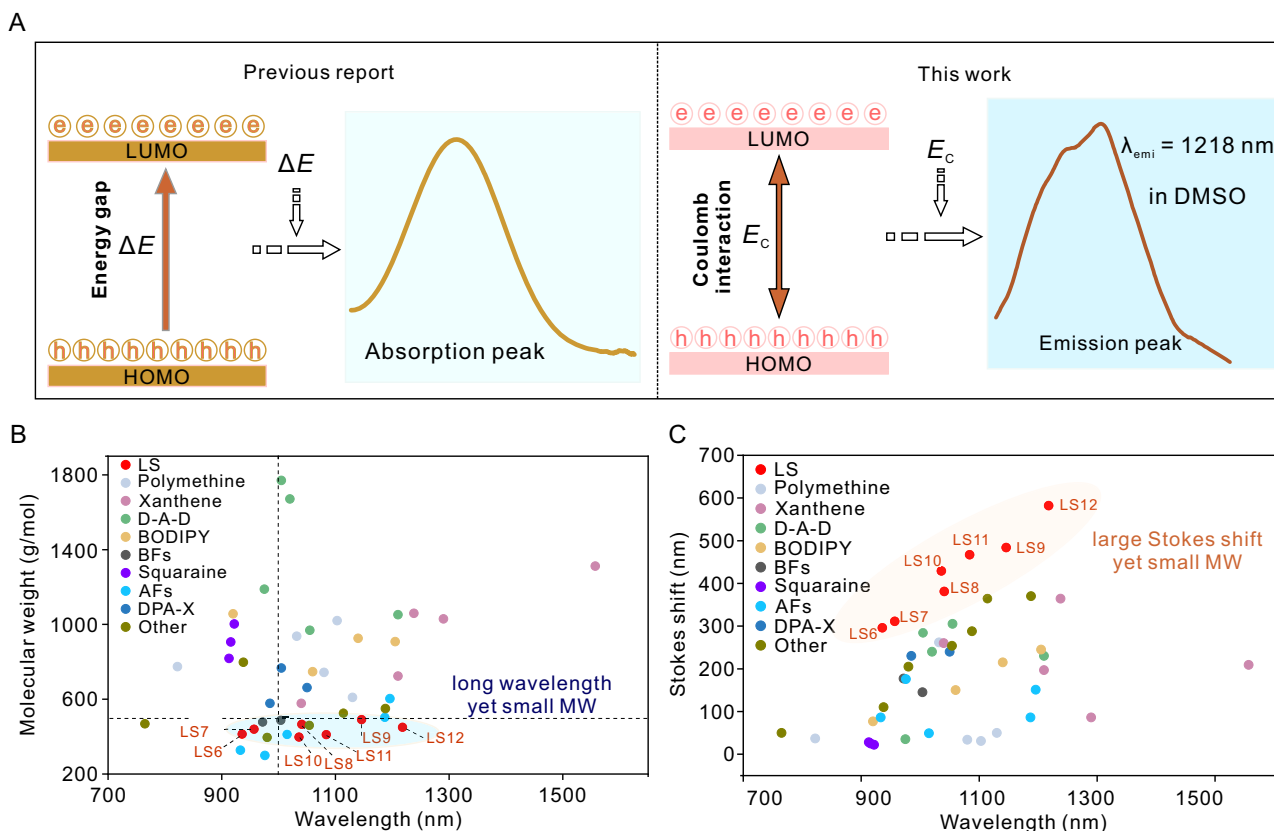
Fig. 1 | Design concept of reducing the Coulomb attraction interaction (E_c). A Design of low-molecular-weight NIR-II dyes by reducing E_c[33]. **B** Relationship between emission wavelength and molecular weight (MW) of various reported NIR-II dyes. **C** Relationship between Stokes shift and MW of various NIR-II dyes. All dyes are labeled and classified, and their corresponding chemical structures and properties are shown in Figs. S2, S3 and Table S19.

Table 1 | The optical properties summary of LSs dyes

LS dyes	E_{HOMO}/E_{LUMO}	Gap (eV)	$\lambda_{abs}/\lambda_{em}$[a]	Δλ (nm)	E_c (eV)	Q.Y.[b] (%)	Log P	u (D)	MW (g/mol)	K_d (nM)	Fold[c]
LS1	−5.52/−2.28	3.24	377/444	67	5.25	1.12	1.39	3.63	226.11	n.a.	n.a.
LS2	−4.95/−1.83	3.12	427/494	67	5.16	0.59	1.62	6.42	243.14	n.a.	n.a.
LS3	−4.82/−2.07	2.74	450/596	146	4.70	0.002	1.50	7.54	269.15	n.a.	n.a.
LS4	−4.71/−2.25	2.46	469/690	221	4.35	0.002	1.32	8.37	295.17	n.a.	n.a.
LS5	−4.68/−2.38	2.30	484/763	279	4.14	0.002	1.25	8.01	321.18	n.a.	n.a.
LS6	−5.09/−3.04	2.05	640/936	296	4.05	0.01	1.12	7.08	413.13	n.a.	1.42
LS7	−4.94/−3.06	1.88	646/957	311	3.74	0.01	1.28	11.52	439.15	660 ± 2.65	22.79
LS8	−4.82/−3.11	1.72	660/1041	381	3.46	0.007	1.34	16.04	465.16	n.a.	2.52
LS9	−4.73/−3.14	1.59	662/1146	484	3.28	0.001	1.41	20.33	491.18	n.a.	2.01
LS10	−5.07/−3.09	1.99	607/1036	429	3.69	0.011	-0.85	23.81	397.20	n.a.	1.90
LS11	−4.93/−3.09	1.83	617/1084	467	3.47	0.007	-0.39	24.60	410.21	n.a.	1.92
LS12	−4.82/−3.11	1.71	636/1218	582	3.29	0.002	-0.19	26.32	449.23	n.a.	2.65

n.a. not available.

[a]The absorbance and emission maxima of LSs (10 μM) in DMSO.

[b]Relative Q.Y. was calculated with IR-26 as a reference (IR-26 = 0.05% in DCE).

[c]Fluorescence increase fold of LSs upon binding with $A\beta_{42}$ fibrils.

To validate this design concept, we first collected the molecular structures and emission wavelengths of 11 classic NIR-II cyanine dyes from the reported literature (Fig. S4)[47]. We investigated the relationship between their NIR-II emission wavelengths and Coulomb attraction interaction. Fortunately, we discovered a correlation between the NIR-II emission wavelength and the Coulomb attraction interaction. A longer emission wavelength corresponds to weaker Coulomb attraction in the dye. Theoretical results confirm the impact of the Coulomb attraction interaction on the NIR-II emission wavelength (Fig. S5).

Encouraged by the above findings, we then used the notable green fluorescent protein (GFP) chromophore (4-hydroxybenzyl diimidazolone, *p*-HBDI, Fig. S6) as a parent scaffold to develop NIR-II dyes by regulating the Coulomb attraction interaction. The impact of structural changes on the Coulomb attraction interaction was systematically investigated by (i) organizing various push-pull electron units on the phenol moiety (electron donor, D1) and the imidazolidinone ring (electron acceptor, A1), and (ii) expanding the π-conjugated system by vinyl bridges. The specific implementation program is divided into three parts: (i) substituting the phenol moiety of *p*-HBDI with hydrogen (H) and *N*, *N*-dimethylamino groups; (ii) introducing electron acceptors (cyano-benzothiazole and 1-methylquinolin-1-ium, A2) or electron donors (4-dimethylaminocinnamaldehyde and 5-[4-(dimethylamino) phenyl]thiophene-2-carboxaldehyde, D2) on the imidazolidinone ring (A1) side of the *p*-HBDI structure; (iii) extending the number of double bonds in D-π-A1 and A1-π-A2 parts. Ultimately, a series of GFP derivatives based on the *p*-HBDI chromophore, featuring D-π-A1 (LS1-5), D-π-A1-π-A2 (LS6-12), and D-π-A1-π-D2 (LSNN, LSNS) structures were constructed (Figs. 2A and S1). The spectroscopic results revealed that the as-prepared GFP dyes with D-π-A1-π-A2 structure exhibited the smallest molecular weight and the longest NIR-II wavelength properties. The detailed synthesis process and the chemical structures of LSs were characterized by ^{1}H NMR, ^{13}C NMR, and HRMS in the Supplementary Information (Figs. S70–128).

Spectroscopic properties of LS dyes

We investigated the spectral properties of the LS family in various organic solvents, summarizing the results in Tables S1–S18. As shown in Fig. S7 and Table 1, all LS1-12 dyes exhibit a broad UV absorption spectrum in common organic solvents, with maximum absorption spanning 300–950 nm. Notably, LS6–LS12 display two distinct absorption bands within this range. The absorption band at shorter wavelengths (300–500 nm), exhibiting lower absorbance, is attributed to the π-π* transition, while the longer wavelength band (600–800 nm), with higher absorbance, represents the ICT process[48]. All LS1-12 dyes exhibit strong emission in various organic solvents, with maximum fluorescence wavelengths extending from the visible to the NIR-II range (444–1218 nm, Fig. S8). The normalized maximum absorption and emission spectral data for LS1-12 are presented in Fig. 2B, C. These dyes possess a tunable long emission wavelength while maintaining a molecular weight under 500 Da, significantly lower than reported commercial and classical dyes (Fig. 1B and Table S19). This property suggests substantial potential for crossing the blood-brain barrier (BBB) and enabling the detection of brain biomarkers. In addition, these dyes also exhibit large Stokes shifts, with the maximum reaching 566 nm, exceeding those of existing commercial dyes (Figs. 1C and S9). This complete spectral separation reduces self-absorption and fluorescence cross-talk interference[49], improving imaging contrast. The large Stokes shifts may result from strong ICT and significant geometric relaxation during photoexcitation.

Given their advantageous properties (long wavelength and low MW), we focused on studying dyes LS6-12. We first assessed their water solubility and observed a gradual increase in the absorbance of LS6-12 with increasing probe concentration (0–50 μM, Fig. S10), which still did not peak at 50 μM, suggesting that these dyes have good water solubility. The photostability of these dyes and ICG was assessed by monitoring fluorescence intensity in DMSO under 808 nm laser irradiation (1 W·cm⁻²). LS6-12 exhibited preferable photostability compared to ICG, making them suitable for long-term fluorescence imaging with minimal bleaching (Fig. S11). We investigated the potential for false positive signals, such as those from intracellular pH variations and the formation of organic dye-protein complexes, during in vivo imaging with these dyes. We tested their fluorescence intensity across different pH, viscosity environments, and in the presence of proteins, including bovine serum albumin (BSA), fetal bovine serum, and human serum albumin. The results showed that none of these potentially interfering components palpable enhanced the fluorescence emissions, suggesting these dyes are promising for in vivo applications (Figs. S12–S16). To evaluate the NIR-II imaging capabilities of LS dyes, 50 μM LS6-12 in a 96-well cell culture plate was imaged at an 808 nm excitation wavelength. The NIR-II fluorescence properties of LS6–12 were captured using a series of long-pass filters (1000–1300 nm LP) covering the NIR-II range (Fig. S17). All dyes displayed intense fluorescence emission wavelengths above 1000 nm, with LS7-10 showing bright NIR-II fluorescence over 1300 nm, indicating their suitability for in vivo NIR-II imaging.

For brain imaging, we also evaluated the physicochemical parameters of LS dyes to assess their potential for crossing the BBB. Generally, molecules with a molecular weight <500 Da, log P < 5, H-bond
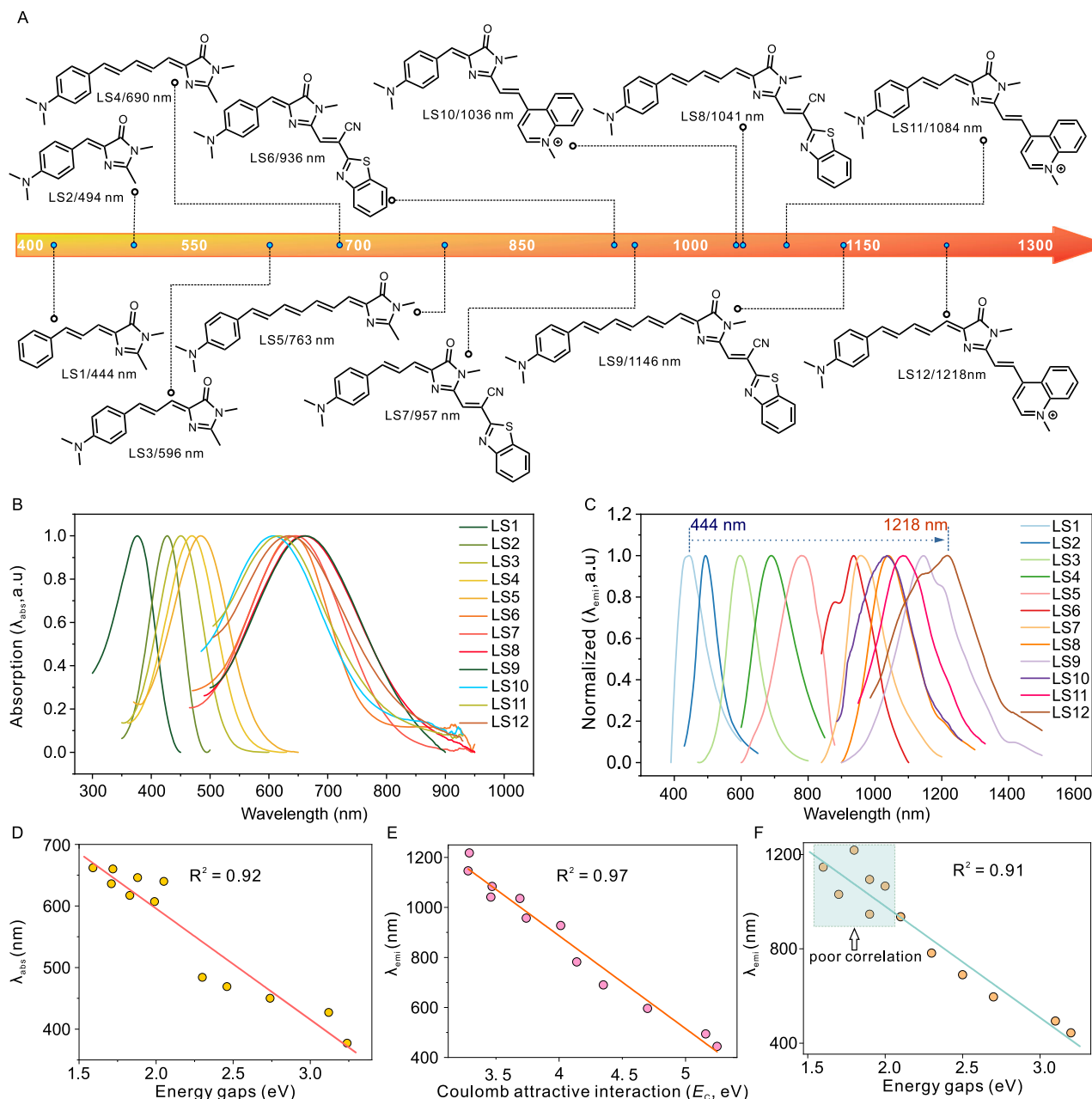
Fig. 2 | Structures, spectra, and structure-property relationships for LSs dyes. **A** The chemical structures of LSs dye. **B** Normalized absorbance spectra of LS1-12 (10 μM) solution in DMSO. **C** Normalized fluorescence spectra of LS1-12 (10 μM) in DMSO. **D** Scatter plot of emission wavelengths *versus* energy gaps for LSs dyes. **E** Scatter plot of emission wavelengths *versus* E_c for LSs dyes. **F** The correlation of emission peaks and the fundamental band gap.

acceptors <10, and H-bond donors <5 are considered likely to exhibit BBB permeability[50,51]. Therefore, we analyzed these key parameters for the LS6-12 fluorophores using a combination of theoretical calculations and experimental measurements of log *P* via the shake flask method[52–54]. The results supported that LS6-9 would exhibit greater BBB permeability than LS10-12 (Table S21 and Fig. S18).

Theoretical computational insights into LSs

We then examine how structural changes impact spectral properties, Coulomb attraction interaction (E_c), and the energy gap (ΔE) by combining experimental data with theoretical calculations, including density functional theory (DFT) and time-dependent DFT (TD-DFT) (Figs. S19–S33 and Supplementary Data 1). Firstly, *N,N*-dimethylamino group was introduced as an electron-rich donor (D) to obtain the D-π-A1 *p*-HBDI-based dye LS3. As shown in Fig. 2, LS3 exhibits a significant

spectral redshift, with absorption shifting from 377 to 450 nm and emission from 444 to 596 nm, alongside a reduced energy bandgap (3.24 eV *vs* 2.74 eV) and Coulomb attraction interaction (5.25 eV *vs* 4.70 eV) compared to LS1. These findings indicate that enhancing donor electron donation plays an important role in reducing energy gaps and Coulomb attraction interaction. The introduction of an electron-rich *N,N*-dimethylamino group is motivated by two key considerations: (1) it acts as an effective electron donor, producing significant spectroscopic redshifts for *para*-substituted aromatic rings and enhancing binding to Aβ[55–57]; (2) its reduced pH sensitivity ensures stable dye performance across varying ambient pH levels, minimizing the risk of false-positive signal interference. On the other hand, an electron acceptor, cyanobenzothiazole, at A2 of the D-π-A1-π-A2 system, along with 1-methylquinolin-1-ium, was introduced to investigate the effect of acceptor groups with varying electron-

withdrawing abilities on the spectra. Taking LS2, LS2QN, and LS10, we showed that the introduction of an additional electron-withdrawing group (A2) in dyes leads to significant bathochromic-shift absorption and emission peaks (Fig. S34).

Our calculations demonstrated that the additional electron-withdrawing group (EWG) caused the reduction of energy gaps and the Coulomb attraction interaction. In this regard, the calculated energy gaps were 3.12 eV, 2.51 eV, and 1.99 eV for LS2, LS2QN, and LS10, respectively. The theoretical Coulomb attraction interaction of LS2, LS2QN, and LS10 were 5.16 eV, 4.23 eV, and 3.69 eV, respectively. By contrast, GFP dyes with D-π-A1-π-D2 (LSNN, LSNS) did not show NIR-II emissions compared with LS6 and LS10 (Fig. S35 and Table S20). The above results indicate that the EWG introduced at A2 position plays a crucial role in modulating the spectral properties of the dyes. Finally, we extended the π-conjugation system of the dyes by incorporating flexible multiple double bonds of varying lengths between the *N, N*-dimethylaniline and imidazolidinone rings (D-π-A1) of the GFP chromophore to further explore the effect of structural changes on the spectral properties. We observed a significant redshift in absorption and emission spectra of LS2–LS5 (494–763 nm), as the number of flexible double-bond chains increased ($n = 1$–4, Fig. 2B, C). Additionally, the effect of EDG/EWG on E_c in *p*-HBDI and LS1-12 was depicted using the electron delocalization index (EDI, Figs. S36 and S37).

The calculation results strongly support the experimental observations. We showed that the energy gaps of LS2–LS5 were 3.12 eV, 2.74 eV, 2.46 eV, and 2.30 eV, respectively. The calculated Coulomb attraction interaction values were 5.16 eV, 4.70 eV, 4.35 eV, and 4.14 eV for LS2–LS5. The data shows a reduction in both the energy gap and Coulomb attraction. However, analysis reveals that regulating E_c has a more significant impact on the redshift of the probe's emission spectrum. Notably, modifying the conjugated polyene chain between D-π-A1 induced a substantial spectral redshift. In addition, our results affirmed that changing the number of double bonds in the π-system of A1-π-A2 also slightly affects the absorption and emission spectra of dyes. For example, the absorption and emission peaks of LSQNN were longer than those of LS3QN (785 nm *cf.* 774 nm, Fig. S38 and Table S20). The calculated energy gap (2.20 eV) and Coulomb attraction interaction (3.20 eV) of LSQNN were lower than those of LS3QN (2.30 and 3.50 eV) (Figs. S32 and S33).

To clarify the impact of energy gaps and Coulomb attraction interactions on the absorption and emission spectra of dyes (Table 1), we plotted the absorption spectra against energy gaps and the emission spectra against Coulomb attraction interactions. As shown in Fig. 2D, we found a strong linear relationship between absorption peaks and energy gap (ΔE) ($\lambda_{abs} = -180.32\Delta E + 956.35$, $R^2 = 0.92$). The absorption peaks redshift as ΔE decreases, consistent with prior reports. We plotted emission peaks against Coulomb attractive interaction (E_C) and observed a superb linear correlation ($\lambda_{em} = -371.18E_C + 2371.3$, $R^2 = 0.97$), which is superior to the correlation between emission peaks and ΔE ($R^2 = 0.91$, Figs. 2E, F and S39). The emission peaks exhibit a significant redshift as exciton E_C decreases, reflecting weaker electron-hole interactions that enhance the ICT effect and increase emission wavelengths. This pronounced ICT effect also elevates dipole moments due to increased charge transfer distance. Our calculations demonstrate a good linear relationship between dipole moments and Stokes shifts ($R^2 = 0.84$), with enhanced dipole moments in LS dyes resulting in substantial Stokes shifts of up to 582 nm (Fig. S40). Based on these data, reducing the Coulomb attraction interaction through structural modification effectively increases emission wavelengths and significantly enhances the Stokes shift of dyes.

In vitro detection of *Aβ42* fibrils with LSs

Inspired by the favorable photophysical properties and physico-chemical parameters of LS dyes, we investigated their potential for specific protein labeling. Abnormal deposition of *Aβ42* in aggregated fibrillar structures (*Aβ42* fibers) is a recognized neuromorphological marker for AD[58–61]. Drawing inspiration from the principle of fluorescent protein bioluminescence, we aimed to harness the hydrophobic cavity of *β*-amyloid to mimic *β*-barrels and enhance fluorescence signals through dye-protein complexes formed by multiple non-covalent interactions for specific detection of *β*-amyloid. Based on Log *P* values, LS6–LS9 demonstrate greater hydrophobicity (Log *P* value: 1.12–1.41) than LS10–LS12 (Log *P* value: −0.85 to −0.19), facilitating better embedding of the dye within the protein cavity. We confirmed this process of *Aβ42* monomer assembly into *Aβ42* fibrils by ThT, particle sizes, and transmission electron microscopy (TEM) (Fig. S41). Consequently, we evaluated the sensitivity of long-wavelength dyes LS6–LS12 to *Aβ42* fibers, respectively. Among them, LS7 exhibits the highest activation signal and the lowest imaging background (*S/N* = 22.79), indicating its potential as an excellent probe for detecting *Aβ42* fibers (Figs. 3A and S42, S43). We successfully established a strong linear relationship between the signal and the concentration of *Aβ42* fibers, demonstrating its quantitative capability for *Aβ42* fibers (Fig. 3B, C). In cuvette studies of NIR-II fluorescence imaging, significant signals were observed even with a 1200 nm long-pass filter (Fig. S44), indicating that LS7 has potential for NIR-II imaging with a high signal-to-background ratio (SBR) for the specific detection of *Aβ42* fibers. Kinetic reaction results supported that LS7 rapidly reacted with excess *Aβ42* fibers, reaching a plateau in fluorescence intensity within 10 min (Fig. 3D). The binding affinity (K_d) value accurately reflects the ability of the probe to bind to *Aβ42* fibers. The K_d value of LS7 and *Aβ42* fibers was 660 ± 2.65 nM, based on the nonlinear relationship between fluorescence intensity and probe concentration (Figs. S45 and S46). The data reveal that LS7 possesses a good binding affinity for *Aβ42* fibrils, enabling dynamic detection of *Aβ42*. Then, LS7 was used to test its ability to competitively displace Thioflavin T (ThT, a standard dye for amyloid staining)-bound *Aβ42* fibrils. As follows, 10 µM ThT was pre-incubated with 50 µM *Aβ42* solution to form the ThT-*Aβ* complex. Subsequently, varying concentrations of LS7 were added to this solution, and fluorescence intensities were recorded at 480 nm for the ThT/*Aβ* complex and at 936 nm for the LS7/*Aβ* aggregates. During the displacement process, we observed a continuous fluorescence decay at 480 nm, along with an increasing NIR-II fluorescence at 936 nm (Fig. 3E). This phenomenon indicated that LS7 effectively displaces ThT from the ThT/Aβ complex, resulting in the formation of the LS7/Aβ complex. These results proved that LS7 presents a much higher binding affinity with *Aβ42* fibrils than ThT. It is important to note that all LS dyes exhibited relatively weak fluorescence signals in the presence of *Aβ42* monomers or oligomers (Fig. S47). To confirm the specificity of LS7 for *Aβ42*, we incubated the probe with potential interferents, including metal ions, amino acids, BSA, and proteases. No significant NIR-II fluorescence emission was observed for all interferents except *Aβ42* fibers, verifying its high selectivity for *Aβ* protofibrils (Fig. 3F). In addition, the probe showed good stability in different cell culture media, substantiating its promising applications in complex cell niches (Fig. S48).

Uncovering sensing principle for LSs and *Aβ42* fibrils

Theoretical calculations were conducted to elucidate the molecular origins of fluorescence quenching for LS6–LS9. Given the observed increase in fluorescence intensity with *Aβ42* fibrils and the presence of multiple rotatable double bonds in LS6–LS9, we propose that twisted intramolecular charge transfer (TICT) may represent a potential fluorescence quenching pathway for these dyes. To verify our inference, we carried out the excited-state potential energy surface scan calculations. Our results demonstrated that LS6–LS9 exhibited two stable conformations in the excited state, and the most stable conformation was exemplified by an approximately 90° rotation between the C-C bond (Fig. 4A–D). Moreover, the rotation barriers decrease
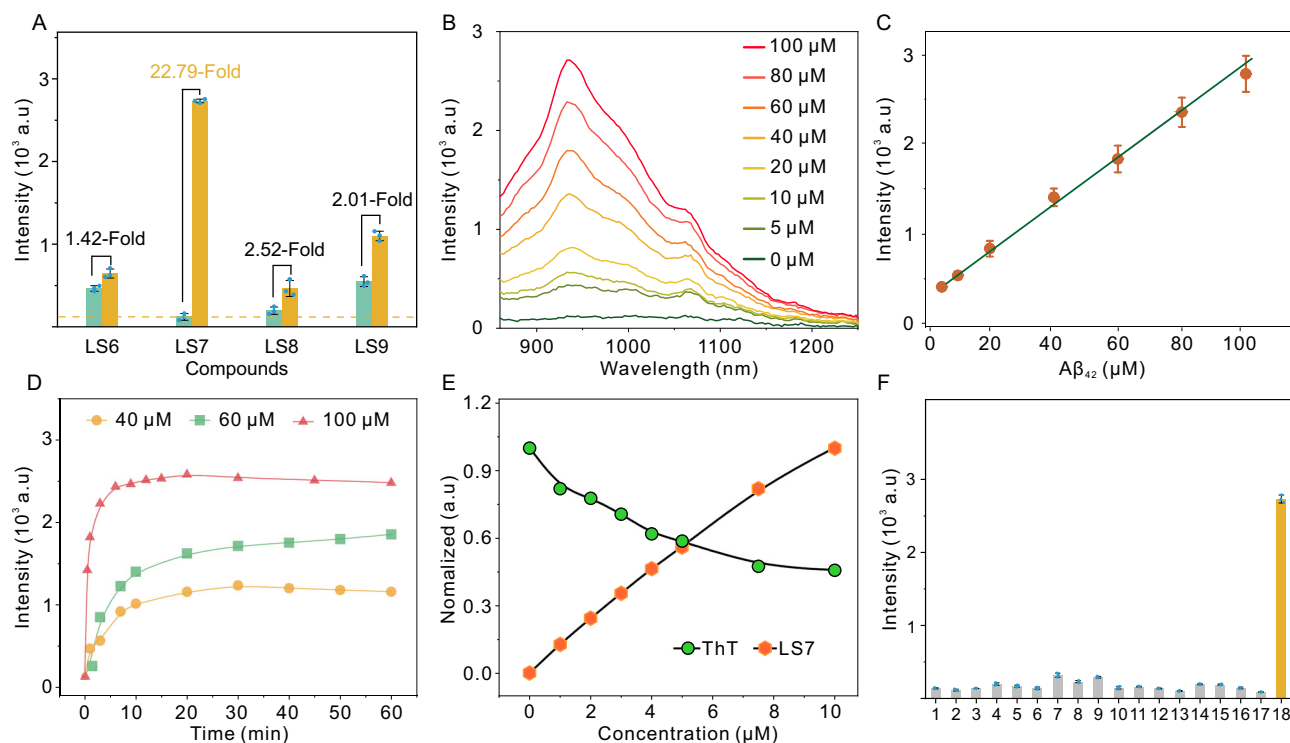
Fig. 3 | $A\beta_{42}$ fibrils sensing of LS7 in solutions. A Fluorescence signal ratio of LSs before and after binding to $A\beta$ fibrils. **B** Fluorescence spectra of LS7 reacted with 0–100 μM $A\beta_{42}$ fibers. **C** Linearly fluorescence response of LS7 to 0–100 μM $A\beta_{42}$. **D** Fluorescence intensities of LS7 (10 μM) at 936 nm against time after addition $A\beta_{42}$ (40, 60, and 100 μM). **E** LS7 (0–10 μM) displaces ThT from the ThT/$A\beta$ aggregation complex and forms the LS7/$A\beta$ aggregation complex. **F** Specificity test for LS7 and various: (1–3) 500 μM Cu^{2+}, Fe^{2+}, K^+; (4–6) 50 μM H_2O_2, HOCl, $ONOO^-$; (7–10) 500 μM L-phenylalanine, glycine, lysine, serine; (11–14) 500 μM trypsin, hyaluronidase, glucose oxidase, horseradish peroxidase; (15–16) 300 μM BSA, HAS; (17) LS7 only; (18)100 μM $A\beta_{42}$ fibers. All the above experiments were performed in PBS (pH 7.4, 10 mM) at 37 °C, λ_{ex} = 808 nm, λ_{em} = 1000–1700 nm. For (**A**, **C**, **F**), data are presented as mean ± SD (n = 3 independent experiments).

with the extension of conjugation units from LS6 to LS9 (Fig. 4E). The rotations of 90° lead to the difference in electronic structure. Take LS7 for instance, at stable conformation, the electron and hole were located on the supplying and pulling electron subunits, respectively. This complete hole–electron separation leads to negligible oscillator strength (f = 0), indicating that this state of LS7 is non-emissive (Fig. 4F). These features are fully consistent with the TICT mechanism. Hence, the fluorescence quenching of LS6–LS9 was ascribed to the formation of TICT states. Next, classical molecular dynamics (MD) was employed to clarify the difference in the fluorescence turn-on ratio of LS6-LS9 for $A\beta_{42}$ fibrils. The GAFF2 force field is used to describe these atoms on the LS6–LS9, and the corresponding atom types are given in Fig. S49. Partial charges of the atoms are obtained by performing quantum mechanics calculations. The geometry optimization and electrostatic surface potential (ESP) charges of the LS6–LS9 are implemented at the Hartree-Fock and ωB97XD calculations based on the 6-31 G* basis sets, and the partial atomic charges are fitted by following the multi-orientational restrained electrostatic potential (RESP) protocol (Figs. S49 and S50). The fibril template that we use to in-silico study the binding mechanisms of $A\beta$ protein and the LS6-LS9 is the $A\beta_{42}$ fibril (Protein ID: 5OQV). Druggability assessment is conducted on the fibril protein to determine three potential active regions via the DoGSiteScorer web server (https://proteins.plus)[62] (Fig. S51a). To avoid simulation discrepancies arising from different initial configurations, we place LS6, LS7, LS8, and LS9 together on purpose to constitute a molecule (Fig. S51b). Later, the AutoDock4 package is employed to predict the docking modes of the LS6-LS9 in the vicinity of the three potential active regions on the $A\beta_{42}$ fibril, thereby resulting in three poses, *viz.* LS6–LS9 (Fig. S51c). Starting from the same initial configurations associated with LS6–LS9 (1–3) in Fig. S51c, we examine the binding behaviors of the $A\beta_{42}$ fibril with each LS6, LS7, LS8, and LS9 in

100-ns atomistic MD simulations (Fig. 4G). Simulation results indicate that for all the LS6-9, only position 3 (LS7) stays still to bind to the $A\beta_{42}$ fibril, whereas positions 1 and 2 (LS6, LS7, and LS8) always make changes in the binding modes. Further, binding free energy (ΔG) is calculated using the molecular mechanics/generalized Born surface area (MM/GBSA) approach[63] to evaluate the affinities of the $A\beta_{42}$ fibril in the binding of LS6–S9, respectively. Analysis of energy for the $A\beta$-complexes shows that as compared to LS6, LS8, and LS9, LS7 exhibits the strongest binding affinities to the $A\beta42$ fibril due to the lowest ΔG value (−4.42 kcal/mol, Fig. S52). Additionally, a configurational analysis was performed for the $A\beta$-complexes to observe the configurational differences in LS6-9 before and after binding (Fig. 4H). From the results, LS6 and LS7 are relatively rigid and have no configuration changes, whereas LS8 and LS9 have a longer -CH- group as a linker and therefore encounter considerable configuration bending. The differences between LS8 and LS9 are that LS8 tends to bend out of plane, while LS9 favors the in-plane bending. Based on the results, the significant fluorescence enhancement of LS7 in the presence of $A\beta_{42}$ fibrils can be attributed to two key factors: the increased ΔG value and the adoption of a planar configuration.

BBB permeability and mapping Aβ plaques

Given LS7 highest SBR in response to $A\beta_{42}$ fibrils in solution, it was selected for further in vivo studies. Initial assessments, including CCK8 assays, blood biochemistry, hemolysis tests, and histopathological analysis of H&E-stained tissue sections, confirmed that LS7 exhibits excellent biological safety (Figs. S53–S57). Subsequently, the activatable fluorescence properties of simulated biological tissues (1% intralipid solution) were investigated at varying penetration depths to assess the imaging potential of LS7 in deep tissues. Co-incubation of the probe with excess $A\beta_{42}$ activated the fluorescence signal, which
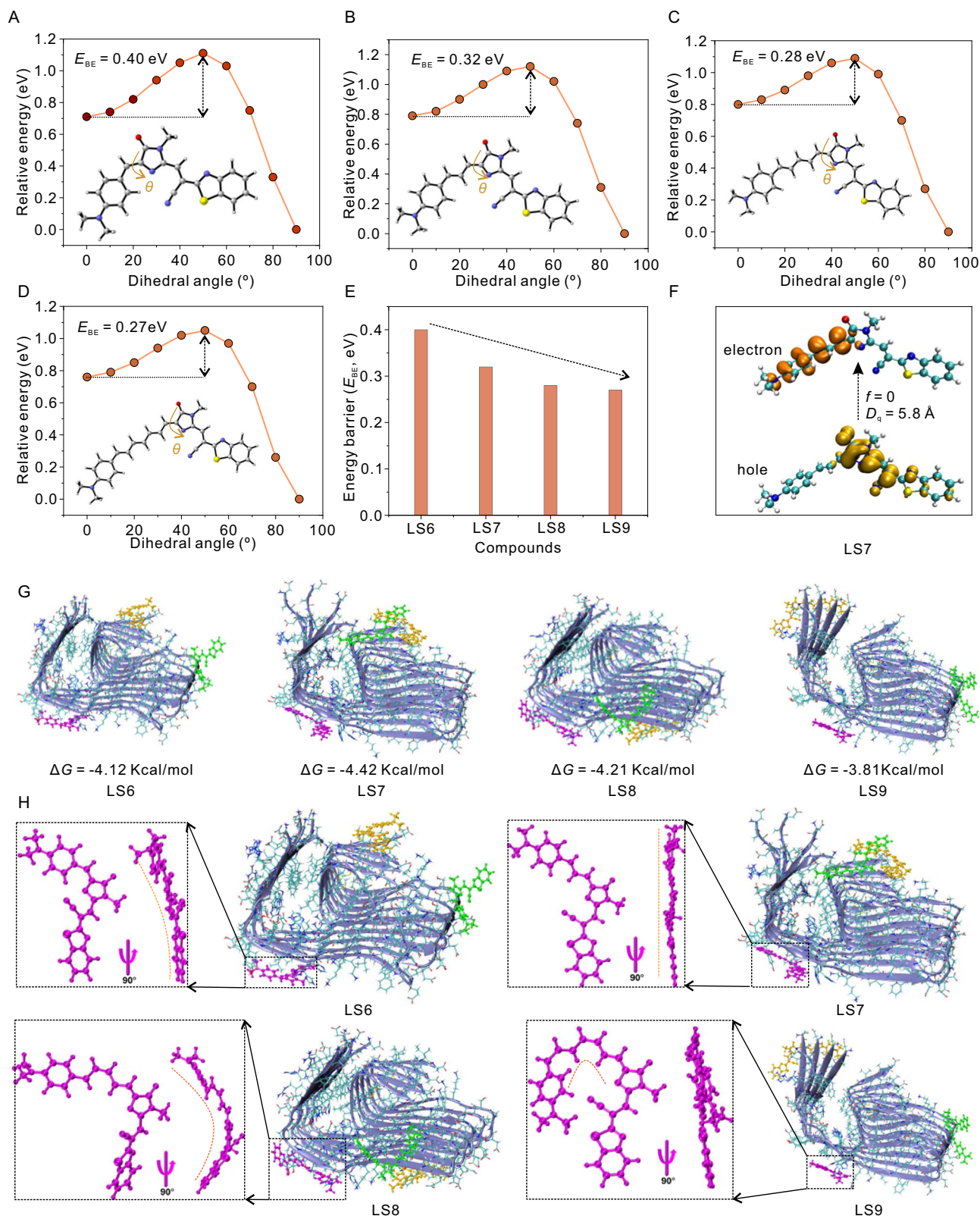
Fig. 4 | Molecular dynamic studies of underlying interaction between $A\beta_{42}$ fibers and LS6-9. The excited-state potential energy surface of (**A**) LS6, **B** LS7, **C** LS8, and **D** LS9. **E** The energy barriers of rotation for LS6, LS7, LS8, and LS9. **F** The distributions of electron and hole in LS7. **G** The binding configurations of $A\beta_{42}$ fibers and dyes along with average binding free energies. **H** The geometrical configurations of LS6, LS7, LS8, and LS9 after binding with $A\beta_{42}$ fibers.

could be resolved at the sharp edge of the capillary up to a depth of 7 mm. Of note, both the activation signal and SBR ratio decreased with increasing intralipid thickness (0–7 mm). Nevertheless, the probe achieved a high SBR of 30.0-fold and an activation ratio of 11.7-fold,

attributed to its excellent imaging contrast in the NIR-II region, along with significantly suppressed background signals and reduced photon scattering (Fig. S58). Shake flask experiments indicated that LS7 exhibited superior lipophilicity compared to ThT (log P: 1.28 vs −0.14),
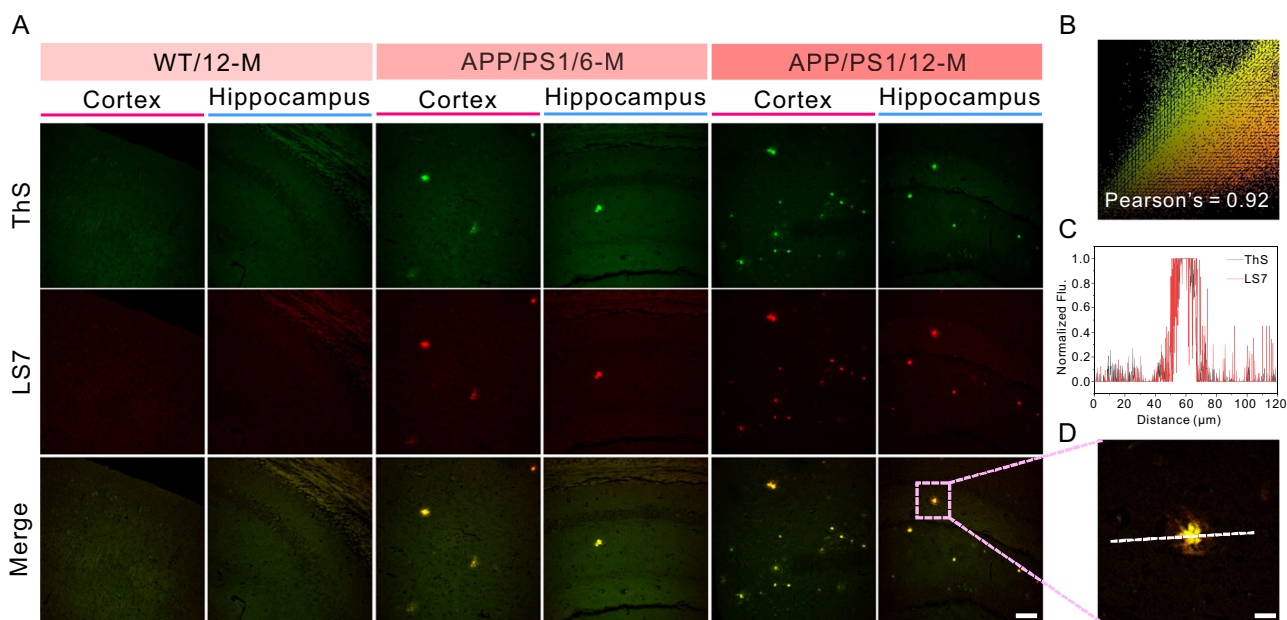
Fig. 5 | Aβ plaque staining in brain slices with LS7. A Histological staining of the brain slices from the hippocampus region and the cortex region of WT or APP/PS1 mice using ThS (λ_{ex} = 405 nm; λ_{em} = 415–500 nm) and LS7 (λ_{ex} = 458 nm; λ_{em} = 555–735 nm), respectively. Scale bar: 50 μm. The experiment was repeated three times independently with similar results. **B** Co-localized images and coefficients of Fig. 5D. **C** The intensity profiles of ThS (black line) and LS7 (red line) in the linear regions of interest (ROI) in (**A**). **D** Merged images of ThS and LS7 channels, fine image of Aβ plaque under magnification, where green for the ThS and red for LS7. Scale bar: 10 μm.

suggesting a greater potential to traverse the BBB[64]. In this regard, we assessed the imaging capability of LS7 for detecting Aβ plaques ex vivo. Brain tissue sections from 6- and 12-month-old APP/PS1 transgenic AD model mice and 12-month-old wild-type (WT) mice were stained with LS7 and ThS (a commercial Aβ plaque dye). No significant plaque staining was detected in the brain sections of 12-month-old WT mice with either LS7 or ThS (Fig. 5A). In contrast, ThS and LS7 staining of brain sections from AD mice of various ages revealed clear fluorescent labeling of plaque aggregation in the cortical and hippocampal regions, with plaque numbers increasing with age. Additionally, the staining areas of Aβ plaques in the same brain region were identical for both LS7 and ThS (Pearson's coefficient: 0.92, Fig. 5B, C). Similar phenomena were observed when Aβ aggregates were stained with anti-β-amyloid 6E10 antibody using immunofluorescence (Fig. S59). Under high magnification (63×), the Aβ plaques displayed a flower-like morphology, with filamentous fibers radiating outward from the center, resembling a spiderweb (Figs. 5D and S60). Furthermore, quantitative fluorescence intensity analysis and a co-localization coefficient (Pearson's coefficient = 0.92) confirmed the consistent staining of Aβ plaques by both LS7 and ThS. These results indicate that LS7 specifically stains Aβ plaques in the brain tissues of AD mice. In conclusion, LS7 NIR-II fluorescence emission, small molecular weight (439 Da), and favorable physicochemical properties enable effective crossing of the BBB and specific detection of Aβ plaques, highlighting its significant potential for in vivo Aβ imaging in AD brains.
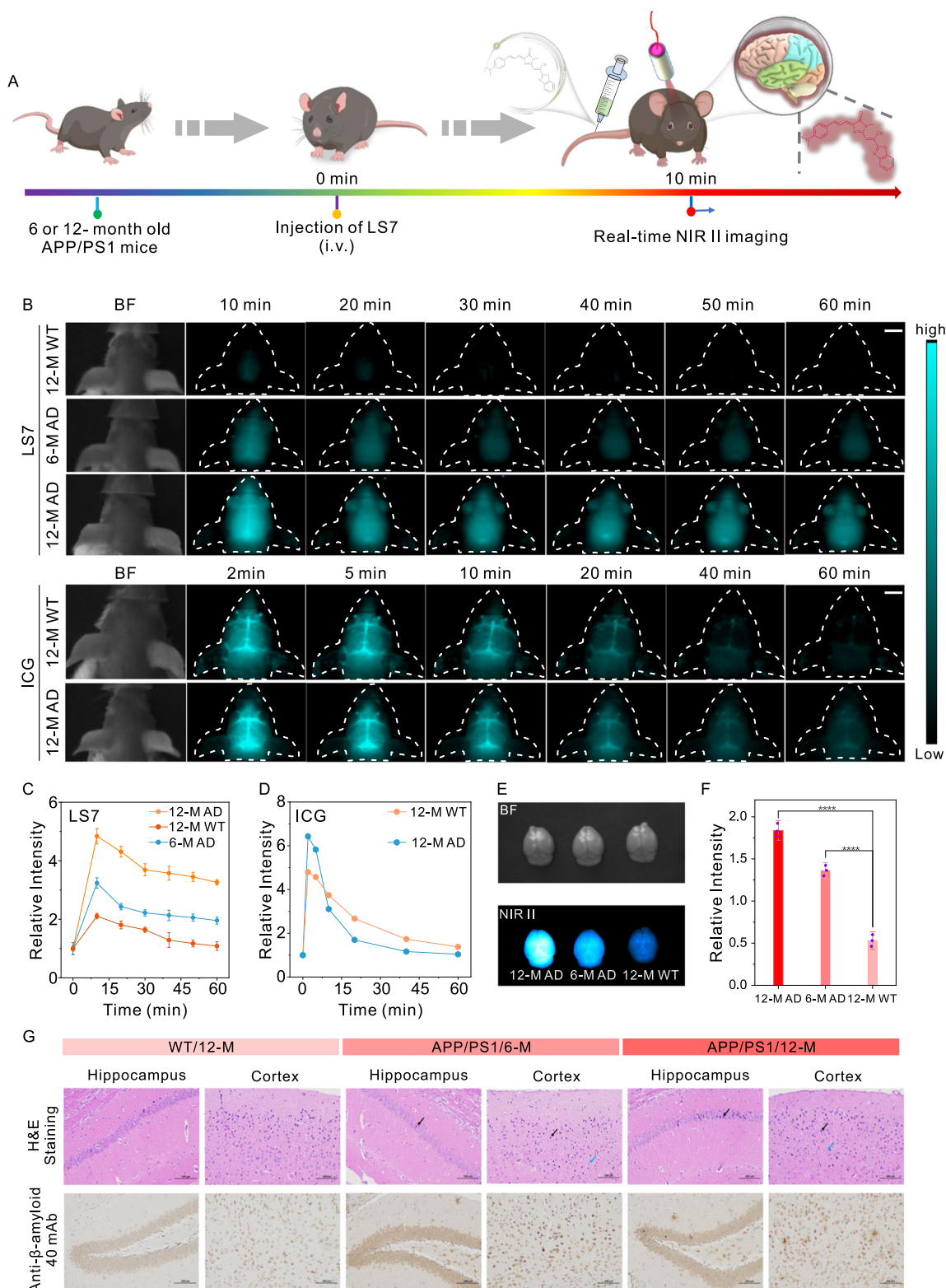
In vivo NIR-II imaging of AD brains

Alzheimer's disease, a neurodegenerative disease characterized by memory loss, cognitive decline, and language impairment, has a complex pathogenesis and is still beyond efficient treatment[65]. The abnormal deposition of β-amyloid (Aβ) plaques in the cerebral cortex and hippocampus is a key pathological hallmark of AD development[66–69]. Thus, real-time visualization of Aβ plaques in the living brain will contribute to our understanding of AD pathogenesis. Encouraged by in vitro solution experiments as well as brain slice-specific imaging of Aβ plaques, we further explored LS7's feasibility of in vivo imaging of Aβ plaques. Firstly, we performed in vivo imaging

studies using 6 and 12-month-old APP/PS1 transgenic AD model mice and 12-month-old WT mice, respectively. As shown in Fig. 6A, NIR-II fluorescence signals were intermittently acquired from the brains of both AD and WT mice at periods of 10 and 300 min following intravenous injection of LS7. The NIR-II fluorescence signal in the brains of WT mice was minimal at all time points post-LS7 injection compared to the AD mice (Fig. 6B). By contrast, in the 6- and 12-month-old AD mice, a clear NIR-II fluorescence signal could be observed at the 10th min after injection, and it slowly entered the brain parenchyma from the brain vasculature and clearly outlined the shape of the mouse brain over time.

The fluorescence signals of AD mice were 1.5 and 2.3 times higher than those of WT mice, respectively (Fig. 6C). In comparison to WT mice, significant NIR-II fluorescence signals were consistently detected in the brains of AD mice up to 240 min after LS7 injection (Figs. S61–S63). The results showcased that LS7 effectively crosses the BBB, binds specifically to Aβ plaques, and prolongs probe retention in the AD mouse brains, enhancing real-time imaging of Aβ plaques. To confirm that the observed NIR-II fluorescence signal originated from AD brain tissue, we sacrificed the mice 30 min after LS7 injection and collected NIR-II fluorescence signals from the isolated brain tissue using an in vivo imager. Fluorescence signals from isolated brain tissues of AD mice at various ages were higher than those from WT mice, and the quantitative analysis closely aligned with the in vivo imaging results (Fig. 6E, F). Next, we conducted NIR-II fluorescence imaging using age-matched WT and AD mice following tail vein injection of ICG. As a control, ICG effectively visualized the blood vessels in the mice's heads within 2 min post-injection (Fig. 6B, D). However, fluorescent signals in the brain diminished over time and eventually disappeared at 40 min, likely due to the fast metabolism of ICG from the cerebral vasculature (Figs. S64 and S65). These results suggested that ICG cannot effectively cross the BBB to reach the brain parenchyma and bind to Aβ plaques, even in AD mice. Subsequently, the brain tissues of the above mice were homogenized and analyzed via HRMS. HRMS spectra revealed a prominent high molecular weight peak for LS7, while no m/z peaks for ICG were detected (Figs. S66 and S67). These results provide strong evidence that LS7 can cross the BBB and

Fig. 6 | NIR-II imaging of AD mouse brains. A Schematic diagram of NIR-II imaging of *Aβ* plagues in AD mice, created by Hangzhou Sphere Ltd. **B** NIR-II brain imaging before and after intravenous injection of LS7 or ICG in WT and APP/PS1 mice at various ages and time points. 1000 nm LP filter. **C** Plot for time-dependent NIR-II fluorescence change of mouse brains post-injection of (**C**) LS7. **D** Plot for time-dependent NIR-II fluorescence change of mouse brains post-injection of ICG. **E** Ex vivo NIR-II fluorescence images for isolated WT and AD brains post-injection of LS7 for 30 min. **F** Intensity for image E. Data are presented as the mean ± SD (*n* = 3 independent biological samples) and analyzed by one-way ANOVA, ****$P < 0.0001$. **G** H&E staining and immunohistochemistry results of the WT and APP/PS1 brain tissues with different months of age. The experiment was repeated three times independently with similar results.

specifically bind to $A\beta$ plaques in AD brains. Finally, H&E staining revealed significant histiocytic lesions in the hippocampal heel cortex region of the AD mouse brains (Figs. 6G and S68). Further, we performed immunohistochemical staining of $A\beta$ aggregates with anti-β-amyloid 40 mAb antibody to confirm the presence of $A\beta$ aggregates in AD mouse brain slices. $A\beta$ aggregates were not observed in WT mouse brain slices, but staining for $A\beta$ aggregates was prominent in AD brain slices of various ages, with this difference evident at all time points (Fig. S69). These in vitro histologic staining results confirm that the probe LS7 effectively detects $A\beta$ plaques in AD brains, corroborating the presence of significant $A\beta$ plaque aggregation in AD mouse brains. This Histochemical finding aligns with the NIR-II fluorescence imaging results.

Discussion

In summary, unlike traditional strategies for NIR-I/II dyes that rely on redshifting absorption wavelengths, we propose an approach that regulates Coulomb attraction interaction (E_c) to directly modulate NIR-II emission for the first time. By virtue of the GFP chromophore, we designed the LS family of GFP-based, NIR emission-tunable dyes by optimizing molecular structure to modulate Coulomb attraction interaction. Leveraging this strategy, the LS dye family achieves long-wavelength emission (444–1218 nm) while maintaining a small molecular weight (226–449 Da) and a large Stokes shift (up to 582 nm). Further, the effectiveness of reducing the Coulomb attraction interaction to develop NIR-II dyes was experimentally and theoretically verified using 18 LS dyes and 11 reported cyanine-based NIR-II dyes. This approach overcomes the longstanding challenge in developing NIR-II dyes—combining long emission wavelengths with small molecular sizes.

LS6-12 are excellent low-molecular-weight NIR-II dyes, with LS6-9 displaying suitable water-solubility, favorable lipophilicity, and excellent BBB permeability, making them potential candidates for brain NIR-II imaging. Additionally, inspired by the fluorescence mechanism of GFP, LS6-9 utilizes the TICT effect to transition from a non-fluorescent to a fluorescent state upon binding to the hydrophobic cavity of β-amyloid, facilitating the detection of $A\beta_{42}$ fibrils. As proof of concept, LS7 enabled real-time NIR-II imaging of overexpressed $A\beta$ plaques in the brains of AD mice. These results demonstrate that reducing the Coulomb attraction interaction can serve as a general guideline for developing next-generation NIR-II dyes.

Methods
Materials and apparatus

Iodomethane, benzothiazole-2-acetonitrile, N-acetylglycine, 4-dimethylaminobenzaldehyde, ICG were purchased from Aladdin Reagent Co. (2E,4E)-5-(4-(dimethylamino)phenyl)penta-2,4-dienal was purchased from Shanghai Bidde Medical Technology Co., Ltd. 4-Quinolinecarboxaldehyde, 4-(dimethylamino)cinnamaldehyde, selenium dioxide were purchased from Sigma–Aldrich. 2-(2-methoxy-4-nitrophenyl)-3-(4-nitrophenyl)-5-(2,4-disulfonic acid benzene)-2H-tetrazolium monosodium salt (CCK8), and other reagents were purchased from commercial suppliers and used without further purification. The ^{1}H-NMR and ^{13}C-NMR spectra were acquired over a Bruker Advance III HD 400 spectrometer. Absorption spectra were recorded on a UV–vis-NIR spectrophotometer (HITACH UH4150, Japan). NIR-II fluorescence spectra were excited by an 808-nm laser (Beijing Hi-Tech Optoelectronic Co., Ltd) and recorded with a fluorometer (Fluorolog-3, Horiba Jobin Yvon, France). In vivo NIR-II fluorescence images were acquired by In Vivo Master NIR-II fluorescence imaging system (Grand Imaging Technology Co. Ltd, Wuhan).

Synthesis

Detailed synthesis steps and characterization results are given in the Supplementary Information.

The measurement of lipophilicity (Log P)

Lipophilicity was determined by the typical flask-shaking method. Briefly, 10 μM probes (from LS1 to LS12) in a mixture solution of ultrapure water and 1-octanol (1:1, v/v) were shaken evenly for 72 h, and centrifuge at 278 × g for 5.0 min. The contents of the probe in water and 1-octanol were measured by UV-vis spectrophotometry. Log P was calculated by the following formula: log P = log (c_o/c_w), in which c_w stands for the probe content in the aqueous phase and c_o stands for the probe content in the organic phase.

Fluorescence studies upon binding to $A\beta$ fibrils

A solution of 0–100 μM $A\beta_{42}$ was added to the mixture containing LS6–LS9 (10 μM in PBS) in a final volume of 200 μL. All emission spectra were obtained after 30 min. stirring at room temperature. Note: all data were measured under the same batch of $A\beta_{42}$ fibrils prepared.

In vitro fluorescent staining of brain slices

Paraffin-embedded 10 μm brain tissue sections from APP/PS1 transgenic mice (C57BL6, APP/PS1, 12-month-old, male) and age-matched wild-type mice (C57BL6, 12-month-old, male) were used for in vitro fluorescent staining. Before staining, the slices were deparaffinized by washing with ethanol for 5 min after a 15 min immersion in xylene. After three times' washing by 50% ethanol (1 min per wash), the slices were incubated in an aqueous solution of LS7(100 μM) for 20 min at room temperature and then washed with ethanol/water (v/v = 40%:60%). After removing the residual liquid with dust-free paper, the slice was then mounted with cover slips. Next, the brain sections were observed using a Leica confocal microscope (TCS SPS CFSMP). To confirm the substantial staining of the plaques, adjacent section of APP/PS1 mice were stained with ThS (10 mg/mL). Antibodies are diluted with a dilution buffer. Samples are first incubated at room temperature to remove the blocking solution, followed by the addition of the primary antibody (1:100–1:10, Purified anti-β-Amyloid, 1-16 Antibody, BioLegend, SIG-39320, or (1:100–1:10, Anti-beta Amyloid 1-40 Rabbit pAb, ServiceBio, GB111197-100) and incubated overnight at 4 °C in a humidified chamber. Wash the slides three times in PBS (pH 7.4) on a decolorization bed, each time for 5 min. After gently drying the sections, add the secondary antibody (Horseradish Peroxidase-labeled goat anti-mouse IgG, ServiceBio, GB23301) and incubate at room temperature for 50 min.

Real-time in vivo imaging in APP/PS1 Mice

APP/PS1 transgenic mice (n = 3, C57BL6, APP/PS1, 12-month-old, male) and an age-matched wild-type mouse (n = 3, C57BL6, 12-months-old, male) were shaved before background imaging and were intravenously injected with LS7 (0.5 mM, 5% DMSO, 95% PBS, 200 μL) and ICG (200 μM, 1% DMSO, 99% PBS, 100 μL). Fluorescence signals from the brain were recorded at different time points after intravenous injection of LS7. For the measurement, a filter set (λ_{ex} = 808 nm, 1000 nm long-pass filter) was used, and optical images were acquired using an exposure time of 1 s. During the imaging process, the mice were kept on the imaging stage under anesthesia with 2.5% isoflurane gas in an oxygen flow (1.5 L•min^{-1}). In vivo NIR-II fluorescence images were acquired by In Vivo Master NIR-II fluorescence imaging system (Grand Imaging Technology Co. Ltd, Wuhan). Imaging data were analyzed by Image J software. All the animal experiments were conducted according to the relevant laws and guidelines and were approved by the Ethical Committee of Hubei University (Approval No. 20240045).

Reporting summary

Further information on research design is available in the Nature Portfolio Reporting Summary linked to this article.

Data availability

The authors declare that all the data supporting the findings of this manuscript are available within the manuscript, supplementary information, and source data files and available from the corresponding authors upon request. Source data are provided with this paper.

References

1. Liu, Y. et al. Versatile types of inorganic/organic NIR-IIa/IIb fluorophores: from strategic design toward molecular imaging and theranostics. *Chem. Rev.* **122**, 209–268 (2022).
2. Chang, B. S., Chen, J., Bao, J. S., Sun, T. L. & Cheng, Z. Molecularly engineered room-temperature phosphorescence for biomedical application: from the visible toward second near-infrared window. *Chem. Rev.* **123**, 13966–14037 (2023).
3. Li, B. H., Zhao, M. Y., Lin, J., Huang, P. & Chen, X. Y. Management of fluorescent organic/inorganic nanohybrids for biomedical applications in the NIR-II region. *Chem. Soc. Rev.* **51**, 7692–7714 (2022).
4. Zheng, Z. et al. Bright near-infrared aggregation-induced emission luminogens with strong two-photon absorption, excellent organelle specificity, and efficient photodynamic therapy potential. *ACS Nano* **12**, 8145–8159 (2018).
5. Hong, G., Antaris, A. L. & Dai, H. Near-infrared fluorophores for biomedical imaging. *Nat. Biomed. Eng.* **1**, 0010 (2017).
6. Lei, Z. & Zhang, F. Molecular engineering of NIR-II fluorophores for improved biomedical detection. *Angew. Chem. Int. Ed.* **60**, 16294–16308 (2021).
7. Li, C., Chen, G., Zhang, Y., Wu, F. & Wang, Q. Advanced fluorescence imaging technology in the near-infrared-II window for biomedical applications. *J. Am. Chem. Soc.* **142**, 14789–14804 (2020).
8. Mu, J. et al. The chemistry of organic contrast agents in the NIR-II window. *Angew. Chem. Int. Ed.* **61**, e202114722 (2022).
9. Chen, Y., Zhang, H., Lei, Z. & Zhang, F. Recent advances in intraoperative nerve bioimaging: fluorescence-guided surgery for nerve preservation. *Small Struct.* **1**, 2000036 (2020).
10. Li, B., Lu, L., Zhao, M., Lei, Z. & Zhang, F. An efficient 1064 nm NIR-II excitation fluorescent molecular dye for deep-tissue high-resolution dynamic bioimaging. *Angew. Chem. Int. Ed.* **57**, 7483–7487 (2018).
11. Antaris, A. L. et al. A small-molecule dye for NIR-II imaging. *Nat. Mater.* **15**, 235–242 (2016).
12. Bai, L. et al. Novel aza-BODIPY-based small molecular NIR-II fluorophores for in vivo imaging. *Chem. Commun.* **55**, 10920–10923 (2019).
13. Zhu, S., Tian, R., Antaris, A. L., Chen, X. & Dai, H. Near-infrared-II molecular dyes for cancer imaging and surgery. *Adv. Mater.* **31**, 1900321 (2019).
14. Wang, L. et al. Benzobisthiadiazole-based small molecular near-infrared-II fluorophores: from molecular engineering to nanophototheranostics. *ACS Nano* **18**, 4683–4703 (2024).
15. Bian, H. et al. Cardiolipin-targeted NIR-II fluorophore causes "avalanche effects" for re-engaging cancer apoptosis and inhibiting metastasis. *J. Am. Chem. Soc.* **144**, 22562–22573 (2022).
16. Liu, J. et al. Precision navigation of hepatic ischemia–reperfusion injury guided by lysosomal viscosity-activatable NIR-II fluorescence. *J. Am. Chem. Soc.* **144**, 13586–13599 (2022).
17. Yang, Q., Ma, H., Liang, Y. & Dai, H. Rational design of digh brightness NIR-II organic dyes with S-D-A-D-S structure. *Acc. Mater. Res.* **2**, 170–183 (2021).
18. Wu, J. et al. The design and bioimaging applications of nir fluorescent organic dyes with high brightness. *Adv. Opt. Mater.* **10**, 2102514 (2022).
19. Zeng, Y. et al. Two key descriptors for designing second near-infrared dyes and experimental validation. *J. Am. Chem. Soc.* **146**, 9888–9896 (2024).
20. Grimm, J. B. et al. A general method to improve fluorophores for live-cell and single-molecule microscopy. *Nat. Methods* **12**, 244–250 (2015).
21. Mao, Z. et al. THQ–xanthene: an emerging strategy to create next-generation NIR-I/II fluorophores. *Adv. Sci.* **10**, 2301177 (2023).
22. Li, J. & Pu, K. Development of organic semiconducting materials for deep-tissue optical imaging, phototherapy and photoactivation. *Chem. Soc. Rev.* **48**, 38–71 (2019).
23. Xu, W., Wang, D. & Tang, B. Z. NIR-II AIEgens: a win–win integration towards bioapplications. *Angew. Chem. Int. Ed.* **60**, 7476–7487 (2021).
24. Qin, Z. et al. NIRII-HDs: a versatile platform for developing activatable NIR-II fluorogenic probes for reliable in vivo analyte sensing. *Angew. Chem. Int. Ed.* **61**, e202201541 (2022).
25. Liu, D. et al. Xanthene-based NIR-II dyes for in vivo dynamic imaging of blood circulation. *J. Am. Chem. Soc.* **143**, 17136–17143 (2021).
26. Ji, A. et al. Acceptor engineering for NIR-II dyes with high photochemical and biomedical performance. *Nat. Commun.* **13**, 3815 (2022).
27. Wei, R. et al. Rigid and photostable shortwave infrared dye absorbing/emitting beyond 1200 nm for high-contrast multiplexed imaging. *J. Am. Chem. Soc.* **145**, 12013–12022 (2023).
28. Li, J. et al. Stable, bright, and long-fluorescence-lifetime dyes for deep-near-infrared bioimaging. *J. Am. Chem. Soc.* **144**, 14351–14362 (2022).
29. Meador, W. E. et al. Silicon-RosIndolizine fluorophores with shortwave infrared absorption and emission profiles enable in vivo fluorescence imaging. *Nat. Chem.* **16**, 970–978 (2024).
30. Zhao, X., Zhang, F. & Lei, Z. The pursuit of polymethine fluorophores with NIR-II emission and high brightness for in vivo applications. *Chem. Sci.* **13**, 11280–11293 (2022).
31. Pan, H.-M. et al. Rational design of asymmetric polymethines to attain NIR(II) bioimaging at >1100 nm. *J. Am. Chem. Soc.* **145**, 516–526 (2023).
32. Aihara, J. -i Reduced HOMO–LUMO gap as an index of kinetic stability for polycyclic aromatic hydrocarbons. *J. Phys. Chem. A* **103**, 7487–7495 (1999).
33. Bredas, J.-L. Mind the gap! *Mater. Horiz.* **1**, 17–19 (2014).
34. Hu, X. M. et al. J-Aggregation strategy toward potentiated NIR-II fluorescence bioimaging of molecular fluorophores. *Adv. Mater.* **36**, 2304848 (2024).
35. Zhang, Q. et al. Bright and stable NIR-II J-aggregated AIE dibodipy-based fluorescent probe for dynamic in vivo bioimaging. *Angew. Chem. Int. Ed.* **60**, 3967–3973 (2021).
36. Tian, Y., Yin, D. & Yan, L. J-aggregation strategy of organic dyes for near-infrared bioimaging and fluorescent image-guided phototherapy. *WIREs Nanomed. Nanobiotechnol.* **15**, e1831 (2023).
37. Zhu, Y. et al. Electron-withdrawing substituents allow boosted NIR-II fluorescence in J-type aggregates for bioimaging and information encryption. *Angew. Chem. Int. Ed.* **62**, e202313166 (2023).
38. Chen, W. et al. Shortwave infrared imaging with J-aggregates stabilized in hollow mesoporous silica nanoparticles. *J. Am. Chem. Soc.* **141**, 12475–12480 (2019).
39. Ma, X. et al. J-aggregates formed by NaCl treatment of aza-coating heptamethine cyanines and their application to monitoring salt stress of plants and promoting photothermal therapy of tumors. *Angew. Chem. Int. Ed.* **62**, e202216109 (2023).
40. Zhao, Q. & He, F. H- and J-aggregation of conjugated small molecules in organic solar cells. *J. Energy Chem.* **93**, 174–192 (2024).
41. Yan, K. et al. Ultra-photostable small-molecule dyes facilitate near-infrared biophotonics. *Nat. Commun.* **15**, 2593 (2024).
42. Leng, H. et al. Dual-emission GFP chromophore-based derivative for imaging and discriminating Aβ oligomers and aggregates. *Anal. Chem.* **94**, 1999–2006 (2022).

43. Baldridge, A., Feng, S., Chang, Y.-T. & Tolbert, L. M. Recapture of GFP chromophore fluorescence in a protein host. *ACS Comb. Sci.* **13**, 214–217 (2011).

44. Paige, J. S., Wu, K. Y. & Jaffrey, S. R. RNA mimics of green fluorescent protein. *Science* **333**, 642–646 (2011).

45. Warner, K. D. et al. A homodimer interface without base pairs in an RNA mimic of red fluorescent protein. *Nat. Chem. Biol.* **13**, 1195–1201 (2017).

46. Wan, W. et al. Covalent probes for aggregated protein imaging via michael addition. *Angew. Chem. Int. Ed.* **60**, 11335–11343 (2021).

47. Cosco, E. D. et al. Shortwave infrared polymethine fluorophores matched to excitation lasers enable non-invasive, multicolour in vivo imaging in real time. *Nat. Chem.* **12**, 1123–1130 (2020).

48. Liu, L. et al. High-resolution imaging of latent fingerprints through near-infrared organoboron AIEgens. *Chin. J. Chem.* **41**, 1465–1470 (2023).

49. Ludwanowski, S., Samanta, A., Loescher, S., Barner-Kowollik, C. & Walther, A. A modular fluorescent probe for viscosity and polarity sensing in DNA hybrid mesostructures. *Adv. Sci.* **8**, 2003740 (2021).

50. Zhang, T. et al. Near-infrared aggregation-induced emission luminogens for in vivo theranostics of Alzheimer's disease. *Angew. Chem. Int. Ed.* **62**, e202211550 (2023).

51. Gong, J. et al. Diaminonaphthalene boronic acid (DANBA): new approach for peroxynitrite sensing site. *Angew. Chem. Int. Ed.* **63**, e202409295 (2024).

52. Lipinski, C. A., Lombardo, F., Dominy, B. W. & Feeney, P. J. Experimental and computational approaches to estimate solubility and permeability in drug discovery and development settings. *Adv. Drug Del. Rev.* **23**, 3–25 (1997).

53. Wang, S. et al. Photostable small-molecule NIR-II fluorescent scaffolds that cross the blood–brain barrier for noninvasive brain imaging. *J. Am. Chem. Soc.* **144**, 23668–23676 (2022).

54. Wang, P. et al. An activity-based fluorescent probe for imaging fluctuations of peroxynitrite (ONOO⁻) in the Alzheimer's disease brain. *Angew. Chem. Int. Ed.* **61**, e202206894 (2022).

55. Cui, M. et al. Smart near-infrared fluorescence probes with donor–acceptor structure for in vivo detection of β-Amyloid deposits. *J. Am. Chem. Soc.* **136**, 3388–3394 (2014).

56. Liu, X.-Y. et al. Rational design of quinoxalinone-based red-emitting probes for high-affinity and long-term visualizing amyloid-β in vivo. *Anal. Chem.* **94**, 7665–7673 (2022).

57. Miao, J. et al. An activatable NIR-II fluorescent reporter for in vivo imaging of amyloid-β plaques. *Angew. Chem. Int. Ed.* **62**, e202216351 (2023).

58. Villemagne, V. L., Doré, V., Burnham, S. C., Masters, C. L. & Rowe, C. C. Imaging tau and amyloid-β proteinopathies in Alzheimer's disease and other conditions. *Nat. Rev. Neurol.* **14**, 225–236 (2018).

59. Kung, H. F. The β-amyloid hypothesis in Alzheimer's disease: seeing is believing. *ACS Med. Chem. Lett.* **3**, 265–267 (2012).

60. Fu, W. et al. Rational design of near-infrared aggregation-induced-emission-active probes: in situ mapping of amyloid-β plaques with ultrasensitivity and high-fidelity. *J. Am. Chem. Soc.* **141**, 3171–3177 (2019).

61. Yang, J. et al. Turn-on chemiluminescence probes and dual-amplification of signal for detection of amyloid beta species in vivo. *Nat. Commun.* **11**, 4052 (2020).

62. Volkamer, A., Kuhn, D., Rippmann, F. & Rarey, M. DoGSiteScorer: a web server for automatic binding site prediction, analysis and druggability assessment. *Bioinformatics* **28**, 2074–2075 (2012).

63. Wu, G., Li, J., Yang, J. & Xiao, X. In silico study of the binding of daunomycin and phenylalanine transfer RNA: probe molecular recognition for structure-based drug design. *Mol. Syst. Des. Eng.* **8**, 786–798 (2023).

64. Mallesh, R. et al. High-affinity fluorescent probes for the detection of soluble and insoluble Aβ deposits in Alzheimer's disease. *ACS Chem. Neurosci.* **14**, 1459–1473 (2023).

65. Selkoe, D. J. Resolving controversies on the path to Alzheimer's therapeutics. *Nat. Med.* **17**, 1060–1065 (2011).

66. Knopman, D. S. et al. Alzheimer disease. *Nat. Rev. Dis. Prim.* **7**, 33 (2021).

67. Shin, J. et al. Harnessing intramolecular rotation to enhance two-photon imaging of Aβ plaques through minimizing background fluorescence. *Angew. Chem. Int. Ed.* **58**, 5648–5652 (2019).

68. An, J. et al. Early onset diagnosis in Alzheimer's disease patients via amyloid-β oligomers-sensing probe in cerebrospinal fluid. *Nat. Commun.* **15**, 1004 (2024).

69. Wang, J. et al. A one-two punch targeting reactive oxygen species and fibril for rescuing Alzheimer's disease. *Nat. Commun.* **15**, 705 (2024).

Acknowledgements

Author contributions

M.Y. and Z.M. conceived and designed the study. M.Y., X.W. and J.Z. performed the experiments and analyzed the data. W.C. performed theoretical calculations. W.S., C.W., Z.M. and Z.L. provided the funding. M.Y., W.C. and Z.M. wrote the original draft. Z.L. edited and reviewed the manuscript. M.Ye., X.Wang, and J. Z. contributed equally to this work.

Competing interests

The authors declare no competing interests.

Additional information

Supplementary information The online version contains supplementary material available at https://doi.org/10.1038/s41467-025-63353-x.

Correspondence and requests for materials should be addressed to Weijie Chi, Zhiqiang Mao or Zhihong Liu.

Peer review information *Nature Communications* thanks Zhen Cheng, Chongzhao Ran, and the other anonymous reviewer(s) for their contribution to the peer review of this work. A peer review file is available.

Reprints and permissions information is available at http://www.nature.com/reprints

Publisher's note Springer Nature remains neutral with regard to jurisdictional claims in published maps and institutional affiliations.